The current issue and full text archive of this journal is available at
www.emeraldinsight.com/0961-5539.htm

An unstructured CVFEM and moving interface algorithm for non-Newtonian Hele-Shaw flows in injection molding

Kemelli C. Estacio
Institute of Mathematics and Computer Sciences, University of Sao Paulo, São Carlos, Brazil
Graham F. Carey
Institute for Computational Engineering and Sciences, University of Texas at Austin, Texas, USA, and
Norberto Mangiavacchi
College of Engineering, University of the State of Rio de Janeiro, Rio de Janeiro, Brazil

Received 3 December 2008
Revised 20 August 2009
Accepted 10 September 2009

Abstract

Purpose – The purpose of this paper is to develop a novel unstructured simulation approach for injection molding processes described by the Hele-Shaw model.

Design/methodology/approach – The scheme involves dual dynamic meshes with active and inactive cells determined from an initial background pointset. The quasi-static pressure solution in each timestep for this evolving unstructured mesh system is approximated using a control volume finite element method formulation coupled to a corresponding modified volume of fluid method. The flow is considered to be isothermal and non-Newtonian.

Findings – Supporting numerical tests and performance studies for polystyrene described by Carreau, Cross, Ellis and Power-law fluid models are conducted. Results for the present method are shown to be comparable to those from other methods for both Newtonian fluid and polystyrene fluid injected in different mold geometries.

Research limitations/implications – With respect to the methodology, the background pointset infers a mesh that is dynamically reconstructed here, and there are a number of efficiency issues and improvements that would be relevant to industrial applications. For instance, one can use the pointset to construct special bases and invoke a so-called "meshless" scheme using the basis. This would require some interesting strategies to deal with the dynamic point enrichment of the moving front that could benefit from the present front treatment strategy. There are also issues related to mass conservation and fill-time errors that might be addressed by introducing suitable projections. The general question of "rate of convergence" of these schemes requires analysis. Numerical results here suggest first-order accuracy and are consistent with the approximations made, but theoretical results are not available yet for these methods.

Originality/value – This novel unstructured simulation approach involves dual meshes with active and inactive cells determined from an initial background pointset: local active dual patches are constructed "on-the-fly" for each "active point" to form a dynamic virtual mesh of active elements that evolves with the moving interface.

Keywords Finite element analysis, Flow, Plastics and rubber technology

Paper type Research paper

1. Introduction

One approach to mathematical treatment of fluid flow and transport processes is to start with the associated conservation laws and constitutive relations and construct a relatively general mathematical model that is then simplified to treat a specific

International Journal of Numerical Methods for Heat & Fluid Flow
Vol. 20 No. 6, 2010
pp. 699-726
© Emerald Group Publishing Limited
0961-5539
DOI 10.1108/09615531011056836

application subclass. This strategy is useful in determining models that allow more efficient numerical simulation and also have special analytic solutions for verification purposes. In mold-injection simulations, model simplification arises from the flow geometry which is characterized by a small flow thickness parameter due to the shape of the mold. Applying perturbation theory and asymptotic analysis in terms of the thickness parameter, together with the theory of lubrication leads to a quasi-steady 2D modified Hele-Shaw system for pressure of a viscous fluid (Holm and Langtangen, 1999; Tucker, 1989). In the present work, the isothermal case for generalized viscosity models is investigated during the mold filling process.

Several strategies have been developed to handle numerical simulation of such moving boundary problems that make use of some form of background mesh or, equivalently, of data structure (e.g. connectivity among nodes) in order to discretize the governing equations via finite element, finite volume and other local discretization methods (e.g. see Codina *et al.*, 1994; Estacio and Mangiavacchi, 2007; Holm and Langtangen, 1999; Jiang *et al.*, 2007; Lewis *et al.*, 1997; Zhou and Li, 2001; Zhou and Turing, 2006). These include Eulerian, Lagrangian or other mixed Eulerian-Lagrangian approaches (Estacio *et al.*, 2008; Hirt *et al.*, 1974; Lewis *et al.*, 1997; Li *et al.*, 2005, 2008; Subbiah *et al.*, 1989).

In the present work an underlying pointset is generated as a "background pointset for the mold domain" and dual computational meshes are constructed on local patches dynamically for control volume pressure solution (Baliga and Patankar, 1980, 1983) in the invading fluid region (an active subset of the dynamic mesh). The governing equation for free surface position is iteratively decoupled from this pressure solve step and can be viewed as an extension of a local volume of fluid update method (Hirt and Nichols, 1981) that uses an active cell level set approach localized in a layer at the propagating front. A layered model through the thickness is implemented to accommodate shear-thinning effects in the generalized Newtonian viscosity models (Carey and Chow, 2003; Myers, 2005) and integration through the depth employs a layered quadrature scheme.

An outline of the paper is as follows: in section 2 following we briefly describe the coupled system for the Hele-Shaw problem and the class of generalized non-Newtonian viscosity models considered in the present study. The iterative decoupled algorithm, discretization of the pressure equation, Newton scheme for the shear rate computation and moving free surface scheme are outlined in section 3. Numerical benchmark studies that examine performance, time to fill and the evolving free surface as well as discretization errors and geometric complexities conclude the work.

2. Hele-Shaw model

2.1 Coupled system

For the class of fluid flow problems considered here, model simplification can be achieved both through a perturbation analysis in terms of the thickness parameter and using the disparate time scales associated with injection and pressure relaxation. This leads to a coupled model with a moving front determined from the velocity field during injection and a quasi-static pressure equation due to rapid pressure relaxation. The resulting quasi-steady 2D Hele-Shaw pressure partial differential equation has the form (Hele-Shaw, 1898; Hieber and Shen, 1980):

$$\nabla \cdot S_2 \nabla p = 0, \tag{1}$$

where p is the pressure and

$$S_2 = \int_0^h \frac{z'^2}{\eta} dz', \tag{2}$$

is the "fluidity" for mold thickness $2h$ and generalized Newtonian viscosity $\eta = \eta(\dot{\gamma})$, where $\dot{\gamma}$ is the shear rate. (Here, and in subsequent numerical studies, symmetry with respect to a centerplane $z = 0$ is assumed.)

Integrating the momentum conservation equation through the mold thickness, yields the following implicit relation between velocity and pressure gradient:

$$v_x = -\frac{\partial p}{\partial x}\left(\int_0^z \frac{z'}{\eta} dz' - \int_0^h \frac{z'}{\eta} dz'\right) \quad \text{and} \quad v_y = -\frac{\partial p}{\partial y}\left(\int_0^z \frac{z'}{\eta} dz' - \int_0^h \frac{z'}{\eta} dz'\right), \tag{3}$$

where the viscosity in the integrand depends on velocity gradients for the generalized viscosity models considered here.

Since velocity is proportional to the pressure gradient, while the pressure field does not vary in the gapwise direction, it is convenient to express equation (3) in terms of the depth averaged velocity $\bar{\mathbf{v}}$ with components:

$$\bar{v}_x = \frac{1}{h}\int_0^h v_x \, dz = -\frac{S_2}{h}\frac{\partial p}{\partial x} \quad \text{and} \quad \bar{v}_y = \frac{1}{h}\int_0^h v_y \, dz = -\frac{S_2}{h}\frac{\partial p}{\partial y}, \tag{4}$$

and use these average values to advance the free surface position during mold filling. The location of the evolving free surface during injection is then determined from the solution of a level set transport equation for advection of a passive scalar ϕ:

$$\frac{\partial \phi h}{\partial t} + \nabla \cdot (\bar{\mathbf{v}} \phi h) = 0. \tag{5}$$

Here phase $\phi = 1$ throughout the injected fluid subregion and $\phi = 0$ in the remaining mold region being invaded by the encroaching fluid. The discontinuity contour represents the free surface.

Under the thin injection layer assumption, only pressure and in-plane shear stress play a significant role in the conservation equations, while shear rate is dominated by the transverse velocity gradient contributions (Verhoyen and Dupert, 1998). A more detailed derivation of the corresponding full non-isothermal model can be found in Kenndy (1995), Subbiah *et al.* (1989) or Tucker (1989). Typical boundary conditions for the isothermal Hele-Shaw injection problem are a prescribed inlet flow velocity or pressure together with a zero normal flow boundary condition, which implies zero normal pressure gradient from equation (4), along any impermeable boundary and zero pressure at the evolving free surface of the injected fluid.

Clearly, there, are several layers of weak coupling in the model and these are exploited later to enhance efficiency in a decoupled algorithm. More specifically, the motion of the free surface is determined by the velocity field of this moving surface at the end of each timestep in a local volume of fluid (VOF) calculation. This velocity field can be post-processed implicitly by non-linear solution of equation (4) using the pressure gradient determined from a prior decoupled quasi-static pressure solve of equation (1). The quasi-static pressure equation depends implicitly on the viscosity and therefore the velocity through the coefficient S_2 in equation (1).

2.2 Viscosity models

Physically, viscosity is a fluid property that represents the internal resistance of the material to deform (Helleloid, 2001). Mathematically, viscosity is defined by a relation between shear stress, τ, and shear rate, $\dot{\gamma}$. If this relation is linear, the viscosity is constant and the fluid is classified as a Newtonian fluid. Fluids described by a non-linear relation between the shear stress and shear rate are termed non-Newtonian fluids. In particular, when the viscosity depends on the shear rate only, the fluid is referred to as a generalized Newtonian fluid, and that is the case of most polymers used in injection molding processes.

More specifically, several generalized Newtonian models for viscosity $\eta = \eta(\dot{\gamma})$ have been proposed for flow subject to high shear rate:

$$\dot{\gamma} = \sqrt{\frac{1}{2} D : D}, \tag{6}$$

where $D = \nabla \mathbf{v} + \nabla \mathbf{v}^{\dagger}$ denotes the rate of strain, † indicates the matrix transpose and [:] indicates tensor product.

From experiment, the viscosity curves should fit properly the fluid behavior in four distinct shear rate regimes:

(1) for sufficiently low shear rate, viscosity is essentially independent of shear rate and the material exhibits Newtonian behavior;

(2) at a higher value of shear rate, the dependence of viscosity on shear rate presents a non-linear transition regime (easily noticed in a log-log plot);

(3) after a further increase it moves into a regime where the viscosity can be modeled by a Power-law relation; and

(4) finally, the viscosity curve levels out, and the material tends toward Newtonian behavior once more (Helleloid, 2001; Myers, 2005).

Among available viscosity models, the Carreau and especially the Cross viscosity models exhibit good agreement with observed behavior for certain polymers of industrial interest (Verhoyen and Dupret, 1998). Both viscosity models present the Newtonian plateau at low shear rates and the Power-law asymptote at high shear rates when a log-log plot is used to describe behavior. However, the transition between these two regimes is more rapid with the Carreau model. In subsequent numerical studies, these types of models are compared for Hele-Shaw applications over a set of parameter values in order to simulate the behavior of a real polymer.

The representative generalized Newtonian viscosity models considered here are (Chen *et al.* 1998; Myers, 2005):

(1) *Power-law.* The standard Power-law model describes the viscosity by:

$$\eta = K \dot{\gamma}^{n-1}, \tag{7}$$

where $\dot{\gamma}$ is the shear rate. This model cannot predict the Newtonian plateau, so it is considered inappropriate for fluids that exhibit such behavior at low shear rates.

(2) *Cross model*. The Cross model is described by:

$$\eta(\dot{\gamma}) = \frac{\eta_0}{1 + \left(\frac{\eta_0}{\tau^*}\dot{\gamma}\right)^{1-n}}, \tag{8}$$

where n is the Power-law index, η_0 is the zero-shear viscosity and τ^* is the parameter that defines the transition region between zero shear rate and the Power-law region of the viscosity curve.

(3) *Carreau model*. The Carreau model is typically written in terms of four parameters:

$$\eta = \eta_\infty + (\eta_0 - \eta_\infty)[1 + \lambda^2\dot{\gamma}^2]^{\frac{n-1}{2}}, \tag{9}$$

where η_∞ and η_0 are the limiting viscosities at high and low shear rates. The high shear viscosity is generally associated with a breakdown of the fluid and is frequently set to zero (Myers, 2005).

(4) *Ellis model*. The Ellis model may be written in terms of shear stress τ as:

$$\eta = \frac{\eta_0}{1 + \left|\frac{\tau}{\tau_{1/2}}\right|^{n-1}}, \tag{10}$$

where η_0 is the viscosity at zero shear rate, $\tau_{1/2}$ is the shear stress at which the viscosity is $\eta = \eta_0/2$ and $(n - 1)$ is the slope of the curve $\log[(\eta_0/\eta) - 1] \times \log(\tau/\tau_{1/2})$.

The model parameters for a given fluid are usually determined experimentally. (The experimental data provided by a viscosity measuring instrument for a given fluid is fitted by the chosen viscosity model.) Mathematically, this consists in the determination of the viscosity model parameters that minimize the distance between the model used and the given data. Table I provides parameter values that characterize polystyrene for each one of the models (Chen *et al.* 1998; Myers, 2005).

In Figure 1 the viscosity $\eta(\dot{\gamma})$ fit is graphed against strain rate $\dot{\gamma}$ for the above generalized Newtonian models of polystyrene in a log-log plot. Notice that, excepting the Power-law, all models include the Newtonian behavior, $\eta(\dot{\gamma}) = \eta_0$, in case of low shear rates.

3. Iterative decoupling and discretization

3.1 Decoupled approach

Numerical simulation of the injection-molding process then involves quasi-static approximate solution of equation (1) for the pressure field in concert with advancement

Model	η_0	n	λ	$\tau_{1/2}$	τ^*	K
Carreau	4×10^6	0.4	46.4			
Ellis	4×10^6	3.2		1.26×10^5		
Cross	4×10^6	0.2838			1.791×10^5	
Power-law		0.39				3.5×10^5

Source: Chen *et al.*, (1998); Myers, (2005)

Table I. Parameters of generalized viscosity models for polystyrene

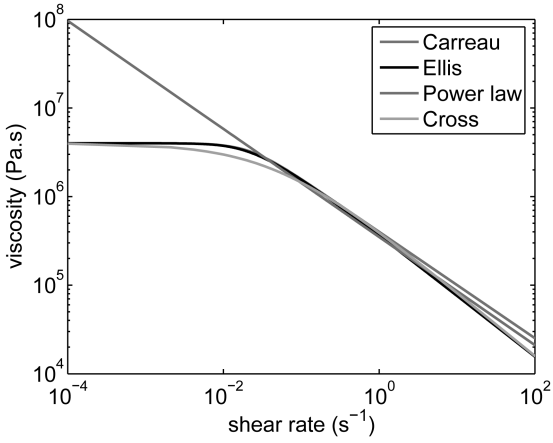

Figure 1.
Comparison plot of generalized Newtonian viscosity models with polystyrene parameters from Table I

of the free surface (Kennedy, 1995) based on equation (5). In the present work an iteratively decoupled strategy is implemented by lagging coefficient dependencies between the respective equations. The main steps in the iterative decoupling and associated linearizations for a typical injection timestep are described as follows. For a given injected domain at time t, and a given decoupled iterate:

(1) *Solve iteratively linearized pressure equation (1) on current domain.* S_2 is calculated from a current iterate of viscosity (such as the Newtonian viscosity at the initial iterate or the current updated viscosity at following decoupled iterates). Using this "current" value of S_2 linearizes the pressure equation, and a pressure approximation is obtained by solving the associated discretized linear equation on the current domain. Then from the pressure solution iterate, the values of velocity components $\overline{v}_x$ and $\overline{v}_y$ are computed in a post-processing step from equation (4) using the current viscosity value iterates. Next, a new value of the shear rate is determined from this average velocity field and the value of the viscosity is updated using this value of shear rate according to the formulas for the generalized viscosity models of equations (7)-(10). The above process is repeated until the variation of the pressure, in two successive iterations, is smaller than a specified tolerance.

(2) *Moving the free surface*. The average velocity from the above computation is used to update the location of the free surface according to the scalar level set equation (5).

Both steps above are repeated until the mold is completely filled.

The following sections present the strategy for constructing the local active dual patches to form a dynamic virtual mesh of active elements and then apply the numerical techniques to solve the fluid flow governing equations (section 3.2). Then, the methodology for solving the pressure equation using the present local mesh control volume finite element method (CVFEM) (section 3.3), the strategy for approximating the shear rate (section 3.4), the timestep selection for the advancement of the free surface using a similar approach applied to the VOF (section 3.5) and a detailed description of the procedures that compute the solution (section 3.6) are also presented.

3.2 Local patch construction

An unstructured node-centered finite volume approach is to be applied on a mesh constructed dynamically from active points (those containing fluid) in a background pointset. In the present work, a sequential local patch construction is implemented that involves defining and ordering neighbor points in a set of overlapping discs centered on the associated active points. The radii of the discs are expressed in the form $c\,l/\sqrt{N}$, where l is a characteristic length of the mold, N is the number of points defining the mold and c is a local scaling parameter for each point that determines a disc covering the adjacent patch as displayed in Figure 2. Moreover, special basis functions may be introduced on the discs to define corresponding so-called meshless methods (Belytschko *et al.*, 1996; Bernal and Kindelan, 2007; Li and Liu, 2002; Liu, 2003).

In the present work, a local triangulation of the points in each disc is constructed to yield a corresponding patch of elements. The "dual" finite volume polygon for this mesh patch centered at interior node i is obtained by connecting the geometric centers of triangles with the median points of "radial" sides. This process is illustrated for a representative disc containing several points adjacent to center point i in Figure 2.

The linearized Hele-Shaw equation is discretized on each finite volume patch as described in the next subsection and solved for the nodal pressure vector.

Remarks. The union of the respective triangulation and polygonal local patches over the domain define a corresponding global finite element-type triangulation and medial node-centered polygonal control volume mesh, but we elect not to construct the global meshes in the present work. Instead the local patches are used to construct "stencils" sequentially and "on the fly." Note that a deficiency of this approach is that the triangulation and dual polygonal mesh may not be optimal with respect to cell shape. For instance, the construction does not yield a Delaunay triangulation except for special pointsets.

3.3 Finite volume formulation

The Hele-Shaw equation (1) for pressure can be written conveniently in divergence form as:

$$\nabla \cdot \mathbf{J} = 0, \tag{11}$$

for flux vector $\mathbf{J} = -S_2 \nabla p$. From the Gauss theorem, the associated conservation

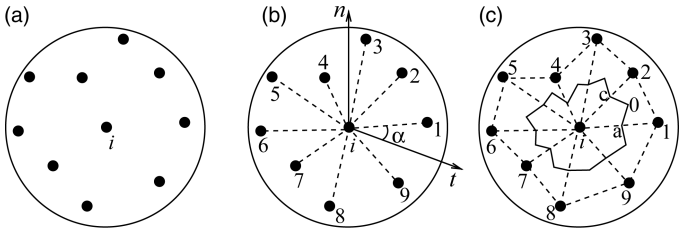

Notes: (a) Disc centered at node i contains neighbor point subset based on disc with a pre-defined radius; (b) neighbors of point i are sorted and ordered; t is a reference vector in the plane defined by the points and n is the vector normal to this plane; (c) triangulation defines the local patch and a virtual control volume follows by median connection

Figure 2.

property on an arbitrary volume satisfies:

$$\int_V \nabla \cdot \mathbf{J}\, dV = \int_S \mathbf{J} \cdot \mathbf{n}\, dS = 0,$$

where S is the boundary of V and $\mathbf{n}$ is a unit outward vector normal to S.

In the discrete CV scheme, this relation on arbitrary volume V in the domain is replaced by the finite dimensional approximation obtained by restricting V to the finite set of control volumes constructed for the specified pointset (Abbassi *et al.*, 2003).

For instance, let us consider a finite volume V_i associated with node point i and let j denote the adjacent neighbors of i; and, for notation simplicity, $j^* = (j+1) \bmod N$, where N is the number of neighbors of point i. Accordingly, in Figure 2(c), $N = 9$ and points $j = 1, \ldots, N$ are associated with point i. Also, for each triangle i-j-j^*, points a and c are the midpoints of segments ij and ij^*, respectively, and point 0 is the geometric center of triangle. Assuming a conforming piecewise linear pressure for the triangles i-j-j^*, the contribution to the patch equation at node i from segment $a0c$ for the surface integral interior to triangle i-j-j^* (with $j = 1$ and $j^* = 2$ for $a0c$) has the form:

$$\int_a^0 \mathbf{J} \cdot \mathbf{n}\, dS + \int_0^c \mathbf{J} \cdot \mathbf{n}\, dS = C_i p_i + C_j p_j + C_{j^*} p_{j^*}, \tag{12}$$

where, for $k = i, j, j^*$, p_k are the values of pressure at the vertices. Coefficients C_k depend on S_2 (which is assumed to be constant over the element at a given time) and on the coordinates of these vertices:

$$\begin{aligned} C_i &= \frac{S_2}{D}[(y_a - y_c)(y_j - y_{j^*}) + (x_a - x_c)(x_j - x_{j^*})], \\ C_j &= \frac{S_2}{D}[(y_a - y_c)(y_{j^*} - y_i) + (x_a - x_c)(x_{j^*} - x_i)], \\ C_{j^*} &= \frac{S_2}{D}[(y_a - y_c)(y_i - y_j) + (x_a - x_c)(x_i - x_j)], \end{aligned} \tag{13}$$

where $D = (x_i y_j + x_j y_{j^*} + x_{j^*} y_i - y_i x_j - y_j x_{j^*} - y_{j^*} x_i)$.

Assembling the contributions of the other elements at node i yields the completed nodal equation with row entries A_{ij}. The resulting system is solved iteratively in subsequent numerical studies by a gradient descent method. Such schemes require repeated matrix-vector (matvec) product and dot product calculations. The more expensive matvec operations are carried out node-by-node in the present formulation, thereby economizing storage. (Similar element-by-element and edge-by-edge strategies have been described for finite element CG algorithms (Carey and Jiang, 1986, 1987; Coutinho *et al.*, 2006)). Diagonal preconditioning is also easily implemented in this scheme (Bridson and Greif, 2006).

3.4 Approximating the shear rate

Recall that the shear rate is defined as:

$$\dot{\gamma} = \sqrt{\left(\frac{\partial v_x}{\partial z}\right)^2 + \left(\frac{\partial v_y}{\partial z}\right)^2}, \tag{14}$$

where the derivatives $\partial v_x/\partial z$ and $\partial v_y/\partial z$ may be analytically obtained though differentiation of the expressions (3) for v_x and v_y. Simplifying:

$$\dot{\gamma} = \frac{z}{\eta}|\nabla p|. \tag{15}$$

Hence, the shear rate varies inversely with the viscosity which in turn depends non-linearly on the shear rate for the generalized fluid models discussed earlier. The resulting non-linear equation is solved iteratively by Newton's method as follows.

Substitute the constitutive relation from (7)-(10) for the viscosity into equation (15) to define the function G:

$$G(\dot{\gamma}) = \dot{\gamma} - \frac{z}{\eta(\dot{\gamma})}|\nabla p|. \tag{16}$$

The corresponding iteration function (Isaacson and Keller, 1966) for Newton's method applied to solve $G = 0$ is:

$$\dot{\gamma}^{k+1} = \dot{\gamma}^k - \frac{G(\dot{\gamma}^k)}{G'(\dot{\gamma}^k)}, \tag{17}$$

where $G'(\dot{\gamma}^k)$ is the derivative of G with respect to $\dot{\gamma}$ evaluated at $\dot{\gamma}^k$.

For instance, expressions for $G(\dot{\gamma})$ and $G'(\dot{\gamma})$ for the Carreau model are given, respectively, by:

$$G(\dot{\gamma}) = \dot{\gamma} - \frac{z}{\eta_0}|\nabla p|\left[1 + (\lambda\dot{\gamma})^2\right]^{\frac{1-n}{2}} \quad \text{and} \quad G'(\dot{\gamma}) = 1 + \frac{z|\nabla p|(n-1)\lambda^2\dot{\gamma}}{\eta_0\left[1 + (\lambda\dot{\gamma})^2\right]^{\frac{n+1}{2}}}.$$

Pressure distribution is constant in the gapwise direction but both shear rate and viscosity vary. Consequently, in the present numerical scheme, the gapwise direction of the mold is divided into N_z layers, and both shear rate and viscosity are approximated piecewise-linearly for each layer: knowing the shear rate at a certain thickness z, a new value for the viscosity of the fluid at the same thickness is established according to the viscosity model chosen.

3.5 Moving the free surface

For approximate identification and advancement of the free surface, a VOF discretization technique (Hirt and Nichols, 1981) is developed to discretize equation (5). In this context ϕ can be interpreted as a "fill factor": if ϕ is equal to 1 at a point of the set, then the control volume associated with that point is assumed to be completely full of fluid; conversely, if ϕ at the point is 0, then the associated control volume is completely empty. Intermediate values of ϕ indicate that the control volume is partially full and may be used to fit the free surface position (Shin and Lee, 2000).

Since the free surface is moving across the background pointset, a local approach for updating the front involves control volumes at the front. The local control volume used for the approximation of the advective transport equation (5) is applied only to points having $0 < \phi < 1$; that is, those points still to be completely filled. The approach is illustrated in Figure 3: Figure 3(a) shows the pointset for the domain, the

position of the free surface and a point i on the free surface. Figure 3(b) isolates the disc for point i and its neighbors; and Figure 3(c) shows the control volume for point i.

Several approaches have been used to discretize equation (5). For example, considering the integral conservation form:

$$\int_V \left(\frac{\partial \phi h}{\partial t} + \nabla \cdot (\overline{\mathbf{v}}\, \phi h) \right) dV = 0, \tag{18}$$

and applying Gauss theorem:

$$\frac{\partial}{\partial t} \int_V \phi h \, dV + \int_S \phi h \overline{\mathbf{v}} \cdot \mathbf{n} \, dS = 0, \tag{19}$$

where S is the boundary of arbitrary volume V and $\mathbf{n}$ is a unit outward vector normal to S.

Now consider a partially filled virtual finite volume V_i associated with node point i, i.e. $0 < \phi_i < 1$. Let j and j^* denote two adjacent neighbors of i forming a typical local triangle i-j-j^* in the associated patch centered at i; for notational simplicity, let $j^* = (j+1) \bmod N$, where N is the number of neighbors of point i. For example, in Figure 2(c), $N = 9$ and points $j = 1, \ldots, N$ are associated with point i as shown. For finite volume V_i, equation (19) implies:

$$\frac{\partial}{\partial t} \int_{V_i} \phi h \, dV = - \int_{S_i} \phi h \overline{\mathbf{v}} \cdot \mathbf{n} \, dS. \tag{20}$$

Since both ϕ and h are approximated as constant in V_i, the left-hand side of equation (20) simplifies accordingly to:

$$h_i V_i \frac{\partial \phi_i}{\partial t} = - \int_{S_i} \phi h \overline{\mathbf{v}} \cdot \mathbf{n} \, dS, \tag{21}$$

where the surface integral contributions are associated with filled neighbor points. For example, for CV boundary segments $a0$ and $0c$ corresponding to neighbors $j = 1$ and $j^* = 2$ of i in Figure 2(c):

$$\int_a^0 \phi h \overline{\mathbf{v}} \cdot \mathbf{n} \, dS = \Phi_j h_j \overline{v}_x (y_0 - y_a) + \Phi_j h_j \overline{v}_y (x_a - x_0), \tag{22}$$

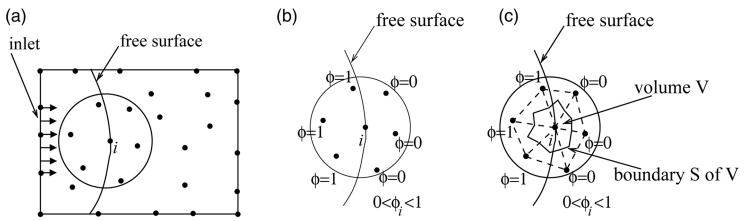

Figure 3.
Determination of local volume V and boundary S associated with point i on the free surface of the fluid

Notes: Only filled points (that is, having ϕ = 1) are used in the advective calculations

$$\int_0^c \phi\, h\, \overline{\mathbf{v}} \cdot \mathbf{n}\, dS = \Phi_{j^*}\, h_{j^*} \overline{v}_x (y_c - y_0) + \Phi_{j^*}\, h_{j^*} \overline{v}_y (x_0 - x_c), \tag{23}$$

where Φ_j is the average value of ϕ_j on $a0$. In this model, it is assumed that the filling factor front is sharp and parallel to $a0$, $\Phi_j = 1$ if $\phi_j = 1$ and $\Phi_j = 0$ if $\phi_j \neq 1$. Analogously Φ_{j^*} is defined for the interface $0c$.

Recalling that point 0 is the centroid of triangle i-j-j^*, equations (22) and (23) can be rearranged so that the right-hand side of equation (21), restricted to triangle i-j-j^*, reduces to:

$$\int_{S_i} \phi\, h\, \overline{\mathbf{v}} \cdot \mathbf{n}\, dS = (E_{ij^*j} \Phi_j + E_{ijj^*} \Phi_{j^*}), \tag{24}$$

where E_{ij^*j} and E_{ijj^*} depend on the coordinates of points and the velocities associated with the virtual finite volumes as:

$$\begin{aligned} E_{ij^*j} &= -\frac{h_j}{6} \left[\overline{v}_x (y_i - 2y_{j^*} + y_j) - \overline{v}_y (x_i - 2x_{j^*} + x_j) \right], \\ E_{ijj^*} &= \frac{h_{j^*}}{6} \left[\overline{v}_x (y_i - 2y_j + y_{j^*}) - \overline{v}_y (x_i - 2x_j + x_{j^*}) \right]. \end{aligned} \tag{25}$$

Equations (22) and (23), and corresponding coefficients E, are calculated for all triangles in the patch for node i. In other words, all neighbors j of point i with $\Phi_j = 1$ contribute to the increasing filling factor of point i and Equation (21) becomes:

$$\frac{\partial \phi_i}{\partial t} = -\frac{1}{h_i V_i} \sum_{j=1}^{N} (E_{ij^*j} \Phi_j + E_{ijj^*} \Phi_{j^*}). \tag{26}$$

Introducing a Forward-Euler scheme with timestep δt, the resulting explicit update formula is:

$$\phi_i^{n+1} = \phi_i^n - \frac{\delta t}{h_i V_i} \sum_{j=1}^{N} (E_{ij^*j} \Phi_j + E_{ijj^*} \Phi_{j^*}). \tag{27}$$

The results of the above calculation may be used to determine the timestep size necessary to fill a control volume associated with any point i that has $0 \leq \phi_i < 1$:

$$\delta t_{fill}\Big|_i = -\frac{(1 - \phi_i^n) h_i V_i}{\sum_{j=1}^{N} (E_{ij^*j} \Phi_j + E_{ijj^*} \Phi_{j^*})}. \tag{28}$$

Choosing δt to be the minimum value of $\delta t_{fill}|_i$ gives the timestep such that only one control volume of the advancing front will be completely filled, and no control volume is overfilled. This implies that a relatively sharp front can be preserved. Hence, this strategy results in a scheme with controlled numerical diffusion, as compared to other VOF methods (Hirt and Nichols, 1981).

The time increment is evaluated at every step of the simulation because of the evolving filling factor field and because control volumes may have different sizes

(Estacio and Mangiavacchi 2007). The update is explicit with corresponding local timestep that depends on the mesh resolution at the front to satisfy a Courant condition for stability and the constraint that ϕ cannot exceed 1. In the later fill post-processing results the computed fill time is taken to be the time to fill all nodes ($\phi = 1$ at all nodes). The approximate fill volume at any time t^n is computed as the accumulated volume for the Voronoi dual patches (see Figure 2(c)) for nodes i that are filled.

3.6 Algorithm

This section presents the main solution algorithm for the discretized, iteratively decoupled system described in section 3. Algorithm 1 computes the quasi-static pressure field approximation, updates the velocity as a decoupled post-processing step and advances the free surface during the mold filling. The main steps are identified by line and action as follows.

Algorithm 1: Solution procedure

Data: Coordinates X,Y,Z of background pointset for the mold geometry and interior.
Result: Pressure and velocity fields during the mold filling.

Assign initial values to h, η_0, S_2 and ϕ;
Set boundary conditions for p;
Set the viscosity model according to Section 2.2;
forall *points* i **do**
  Compute the radius of each point i and find neighbors of i;
  Compute the vector n normal to the plane that contains i and its neighbors j;
  Compute the reference vector t in the plane;
  forall *neighbors* j *of point* i **do**
    Compute angles α_j between vectors ij and t;
  end
  Sort angles α and create a vector nb_s of the neighbors of i sorted according to α;
end
$is\_not\_filled \leftarrow$ true;
while *is_not_filled* **do**
  Select active points;
  convergence_pressure $\leftarrow$ false;
  $it \leftarrow 0$;
  while *(* **(not** *convergence_pressure)* **and** $it < it_{max}$*)* **do**
    forall *neighbors* j *in* nb_s *of active point* i **do**
      Approximate a local value for S_2 as average of S_2 in points i, $nb\_s(j)$ and $nb\_s(j+1)$;
      Compute C_i, C_j, C_{j^*} and D according to equation (13);
      Assemble matrix K with the values of C_i, C_j and C_{j^*};
    end
    Solve linear system for pressure p;
    Determine velocities $\overline{v}_x$ and $\overline{v}_y$ according to equation (4);
    Determine the viscosity according to equations (7) – (10);
    Determine the fluidity S_2 according to equation (2);
    convergence_pressure $\leftarrow$ Check convergence of the pressure field;
    $it \leftarrow it + 1$;
  end
  Determine velocities v_x and v_y according to equation (3);
  Update the free-surface position ϕ according to equation (27);
  Find the new time-step δt according to equation (28);
  $filling\_time \leftarrow filling\_time + \delta t$;
  $is\_not\_filled \leftarrow$ Check if mold is completely filled;
end

In line 5, a radius is associated to each point i in the discretization defining the neighbors of i. The neighbors of i are sorted according to the angle formed from the point j to point i and a reference vector t, as performed in lines 6-11. After the angles are sorted, a new vector *nb_s* is created by sorting the order of the neighbors of i according to these angles and is used to compose the finite volume for applying the CVFEM. Line 14 defines the loop for the timestep: since the present approach uses a VOF method with a timestep constraint based on only one control volume being filled at each timestep, the loop occurs while there is at least one point j having $\phi_j < 1$. Line 15 updates the active points subset as the front moves: inactive points are either empty of fluid or points of prescribed inlet pressure, and do not participate in the calculation. Line 18 displays the loop for pressure convergence with the method of successive approximations. Line 19 performs the assembly of the linear pressure system for equation (1) using equations (12) and (13) for each active point i, according to sections 3.2 and 3.3. Line 24 solves the linear system for the pressure using a conjugate gradient method. Finally, lines 25-27 call procedures for calculating, respectively, the depth average velocity field according to equation (4), the viscosity model, using one of the equations (7)-(10) and the fluidity S_2, according to equation (2).

4. Numerical results

Results of simulations for several test problems are now presented for isothermal flow of Newtonian and non-Newtonian fluids in several flow and mold conditions. First, the computed fill time of the moving front algorithm is used to assess the mass-preserving accuracy of the scheme and code (section 4.1). Then, a complexity analysis with operation counts for the most computationally intensive part of the calculation is presented (section 4.2). Next, the computed solution is compared with a manufactured exact solution for a simple test geometry (section 4.3) and with numerical results from the literature for more complex geometry (sections 4.4 and 4.5).

Remark: For convenience, the pointsets used in the present case studies were generated by Easymesh (Niceno, 2001) from a specified set of points on the boundary. For relatively simple domains and boundary point spacing, the associated Easymesh triangulation yields a relatively equispaced pointset. Other pointset generation techniques are also appropriate. The Easymesh triangulation is not explicitly used in the subsequent mold filling simulations – only the triangle vertices are loaded as the background pointset.

4.1 Fill-time comparison

The exact time needed to fill a mold with constant thickness at a given fixed flow rate can be calculated trivially based on mass conservation in these flow conditions, and is:

$$t = \frac{A}{l\, v_0}, \tag{29}$$

where A is the mold area, l is the inlet region length and v_0 is the injection velocity. This therefore provides a basis for a test of the accuracy of the moving front algorithm in particular, and more generally the mass-preserving accuracy of the overall scheme and code. Other verification tests are also needed (Roy, 2005) and some will be considered subsequently.

Let us then compare the exact fill time for the simple square mold in Figure 4 with horizontal flow velocity specified at the mold inlet as $v_0 = 10^{-1}$ m/s against simulation fill times for a set of three successively finer uniform pointsets defining mold boundaries and interior having 100, 400 and 1,600 points, respectively.

The difference between the exact fill time and the computed fill time for a given pointset is the fill time error and the absolute value of this error can be compared for successively refined pointsets to gauge this global aspect of accuracy and convergence dependence on the discretization. For the equidistributed pointsets of the type used here the pointset is uniform with typical average local patch diameters $l/\sqrt{N}$ in a mold of characteristic length l. The slope of the log-log plot of absolute error against pointset size is analogous to the rate of convergence expected for computations on uniform meshes.

The relation for the observed order of accuracy q in terms of the fill time error l is (Roy, 2005):

$$q = \frac{\log\left(\frac{L_{k+1}}{L_k}\right)}{\log\left(\frac{d_{k+1}}{d_k}\right)}$$

where L_k refers to the error committed in the refined pointset, and L_{k+1} in the coarse one and, similarly, d_k and d_{k+1} are the average local patch diameters, where the discretization error is examined by employing the relative error.

For this test case, the exact filling time is 5 s whereas the present method exhibits convergence from below for fill time with 4.92, 4.96 and 4.98 s for the present scheme with sets of 100, 400 and 1,600 points, respectively. Table II summarizes the data employed for the analysis and the resulting relative error for a Newtonian fluid case. Similar fill time results are obtained for the non-Newtonian viscosities.

Figure 5 illustrates that the order of accuracy obtained is approximately one, since on the logarithmic scale, a first-order scheme displays a slope of unity whereas a second-order scheme displays a slope of two.

For a given mesh the algorithm fills one Voronoi cell at each timestep as described previously. A Voronoi cell centered on node i is "assumed to be filled" when the associated node value $\phi_i = 1$. Hence, one can monitor the fluctuation in fill time error

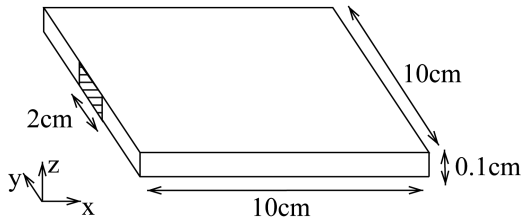

Figure 4.
Mold dimensions and inlet region (in pattern)

Pointset name	Nodes	Diameters (m)	Filling time (s)	Relative error (%)
Pointset 1	100	0.0100	4.925000	1.500000
Pointset 2	400	0.0050	4.968750	0.625000
Pointset 3	1,600	0.0025	4.985937	0.285259

Table II.
Data employed in the convergence study and relative error (%)

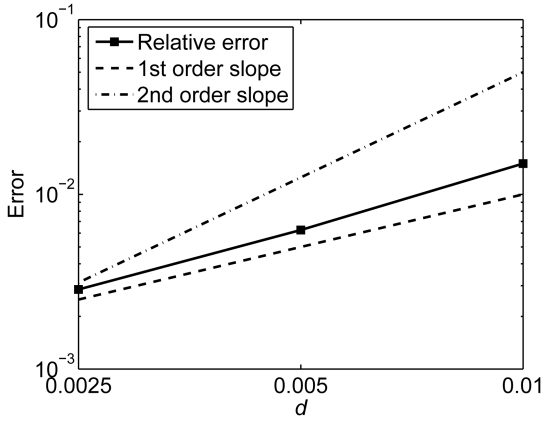

Figure 5.
Relative error committed on the prediction of time filling of a mold and order of accuracy q of the present method

at each timestep of the injection process by using the computed fill volume at the conclusion of a given timestep to infer a corresponding exact time for that volume from equation (29). The procedure for determining when a cell is filled will influence the accuracy at each timestep with larger fluctuations in error on coarser meshes. We summarize the results of this comparison in Table III, which presents the maximum, minimum and mean fill time error values (as a percent error) during the process for each of the three meshes.

4.2 Performance test

Performance data can be achieved either through CPU times or operation count complexity. CPU times are less reliable and depend on the processor, compiler and implementation. Hence we have focused on the complexity and operation counts for the most computationally intensive part of the calculation: the non-linear successive approximation scheme with the conjugate gradient system solves with the non-Newtonian fluid models on the evolving active mesh as the fluid front advances. This is augmented with tabulated numerical performance results for cases computed on two meshes (a coarse mesh and a refined mesh with four times as many node points) and the mold described in section 4.1.

Details of successive approximation counts, conjugate gradient solve steps at each non-linear iteration and local non-linear Newton solves for the viscosity models are tabulated and compared on Table IV for representative timesteps at different fill levels (5, 25, 50, 75, 95 percent) on the two meshes. The conjugate gradient method employed in this case uses incomplete Cholesky preconditioning with no fill-in, with the option of recomputing the preconditioner or fixing the preconditioner for the associated number of successive approximation solves.

Pointset name	Diameters (m)	Maximum error	Minimum error	Average error
Pointset 1	0.0100	5.5464	0.1505	2.1836
Pointset 2	0.0050	3.0855	0.0072	1.3495
Pointset 3	0.0025	1.4315	0.0004	0.7469

Table III.
Measure of error committed throughout the simulation (%)

Model	Pointset	% fill	5%	25%	50%	75%	95%
Carreau	100	<NSA>	6	5	4	5	5
		<NCG>/NUN	7/7	9/27	11/52	14/57	15/97
		<NVI>	7.4	7.0	7.0	7.0	7.0
	400	<NSA>	4	4	3	3	3
		<NCG>/NUN	8/25	13/104	18/204	24/304	26/384
		<NVI>	7.1	6.9	6.9	7.0	7.0
Cross	100	<NSA>	17	10	8	6	10
		<NCG>/NUN	6/7	9/27	10/52	12/60	14/97
		<NVI>	4.7	4.2	4.0	4.0	4.0
	400	<NSA>	12	6	5	5	3
		<NCG>/NUN	8/24	13/104	18/204	23/304	26/384
		<NVI>	4.3	4.2	4.0	4.0	4.0
Ellis	100	<NSA>	11	7	6	5	8
		<NCG>/NUN	6/7	9/27	10/52	12/60	14/97
	400	<NSA>	8	5	4	3	3
		<NCG>/NUN	8/24	13/104	18/204	24/304	26/384
Power-law	100	<NSA>	6	6	3	5	5
		<NCG>/NUN	7/7	10/27	11/52	14/60	15/97
	400	<NSA>	5	4	3	3	3
		<NCG>/NUN	8/24	13/104	19/204	24/304	26/384

Table IV.
Operations count for the successive approximation, conjugate gradient and non-liner Newton (when applies) solve for each viscosity model

Notes: < > denotes average values, NSA denotes the number of successive approximations for the pressure, NCG denotes the number of conjugate gradient iterations for solving the linear system and NVI is the number of iterations of the Newton's method for solving the non-linear viscosity; values obtained for mold in Figure 4 described by 100 and 400 points

In the tabulated values below, the preconditioner is fixed based on the linearized system at the first successive approximation solve at each timestep. This implies more conjugate gradient iterations than the alternative where the preconditioner is reformed after each successive approximation iteration.

4.3 Inlet pressure channel test

Typical boundary conditions for the isothermal Hele-Shaw injection problem are prescribed inlet flow velocity or pressure. During mold filling with a prescribed constant inlet flow velocity, an increasing pressure at the inlet region is anticipated throughout the duration of the simulation. Injection into a simple rectangular mold domain can be compared with the simple analytic solution to a reduced one-dimensional mathematical model to evaluate aspects of the method and software implementation.

Accordingly, we consider injection of a rectangular mold as shown in Figure 6 with constant horizontal flow velocity v_0 specified at the mold inlet until the mold is half-way filled, and compare against an analytical solution for the pressure field.

The mold dimensions do not vary in the x-direction, and slip boundary conditions are applied at the narrow side walls. It follows that:

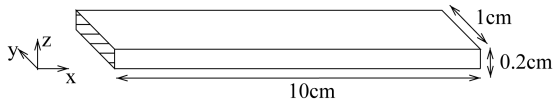

Figure 6.
Dimensions of the channel and inlet region

$$\frac{\partial \overline{v}_x}{\partial y} = 0 \quad \text{and} \quad \overline{v}_y = 0.$$

so the velocity solution in the fluid is simply:

$$\overline{v}_x = v_0 \quad \text{and} \quad \overline{v}_y = 0, \tag{30}$$

and the filling front advances as a plane perpendicular to the x-axis, moving with velocity v_0. From equation (4), the corresponding pressure distribution satisfies

$$\frac{\partial p}{\partial x} = -\frac{h}{S_2} v_0 \quad \text{and} \quad \frac{\partial p}{\partial y} = 0,$$

Integrating, the pressure distribution is the linear function:

$$p = p_{inj} - \frac{h}{S_2} v_0 x,$$

where p_{inj} is the pressure at the inlet.

At the moving free surface $x = \delta l$, $p = p_0$, where δl is the displacement of the free surface and p_0 is the atmospheric pressure, so the inlet pressure is:

$$p_{inj} = p_0 + v_0 \delta l \frac{h}{S_2}. \tag{31}$$

In the case of a Newtonian fluid, the viscosity is constant and therefore the fluidity S_2 is constant so the analytic solution for pressure at the inlet follows immediately. In the non-Newtonian case the non-linear dependence of fluidity on shear rate enters the calculation. Here we consider polystyrene with viscosity behavior modeled by the generalized Newtonian models given in section 2.2. For Carreau and Cross models a non-linear Newton solver is used to compute the shear rate and hence the viscosity for each of the N_z layers through the gapwise direction.

Accordingly, S_2 is computed by vertical piecewise-trapezoidal quadrature through the mold thickness and an approximate pressure at the inlet follows from this calculation with numerical errors arising here from the non-linear scalar solve and layer quadrature. A small tolerance for the Newton iteration and a sufficiently fine layer discretization for the quadrature ensure that these numerical errors are controlled to high precision in approximating the analytic non-Newtonian solution.

This simple analytic result for the inlet pressure is now used in a baseline comparison of the numerical method and code for the stated viscosity models at several different inlet velocities when the mold is half-way filled, i.e. $\delta l = 5 \times 10^{-2}$ m. The background pointset from Easymesh defining mold boundaries and interior has 498 points. In the following tests, four different values of an average shear rate, $\dot{\gamma}_{\text{avg}} = v_0/h$, are considered for each viscosity model. Also, the gapwise numerical integration of S_2 is carried out for different choices of N_z to examine the sensitivity to layer discretization.

Table V gives analytical inlet pressures obtained for each viscosity model at four different values of shear rate. For the analytical solution, viscosity and fluidity are approximated numerically in the gapwise direction using a very fine discretization

($N_z = 1{,}000$ layers) so quadrature error is effectively eliminated. As a comparison, Table VI illustrates the relative error (percent) committed by the CVFEM method, for each viscosity model at the same shear rates, and with 5 and 100 layers in the gapwise direction, respectively.

The smaller error levels for $N_z = 100$ layers are essentially unchanged from those at $N_z = 20$ and hence quadrature error has been controlled so the error tabulated is mainly associated to the spatial discretization. The error committed considering $N_z = 5$ includes both the error due to spatial discretization and the error associated with the numerical integration.

The velocity profiles for molten polystyrene are displayed in Figure 7 at the two extreme values of average shear rate described earlier. For $\dot{\gamma}_{avg} = 10^{-4}$, viscosity is essentially independent of shear rate, and the Carreau, Cross and Ellis models closely approximate Newtonian behavior, therefore the velocity profiles for such models are coincident. The Power-law model does not predict the Newtonian behavior for low shear rates and presents a more flattened profile in the central region. The subsequent increasing values of shear rate leads to a transition region for the viscosity models to the Power-law region. The Cross, Carreau and Ellis velocity profiles flatten out at the center, becoming similar to the Power-law fluid. This is evident when $\dot{\gamma}_{avg} = 10^{2}$.

Table V.
Analytical inlet pressure (*Pa*) of the channel entrance for various viscosity models at four representative values of average shear rate $\dot{\gamma}_{avg} = v_0/h$ when the mold in Figure 6 is half-way filled

Model	10^{-4}	10^{-2}	10^{0}	10^{2}
Carreau	2.9999×10^{4}	2.3714×10^{6}	1.8252×10^{7}	1.1518×10^{8}
Cross	2.9343×10^{4}	1.8592×10^{6}	1.6613×10^{7}	6.4741×10^{7}
Ellis	2.9999×10^{4}	2.3185×10^{6}	1.5284×10^{7}	6.5470×10^{7}
Power-law	4.3567×10^{5}	2.6252×10^{6}	1.5815×10^{7}	9.5314×10^{7}
Newtonian	3×10^{4}	3×10^{6}	3×10^{8}	3×10^{10}

Note: $N_z = 1{,}000$

Table VI.
Relative error of inlet pressure estimation (%) at four values of the average shear rate $\dot{\gamma}_{avg}$

Model	N_z	10^{-4}	10^{-2}	10^{0}	10^{2}
Carreau	5	3.0068	3.0573	1.9614	1.7277
	20	0.0012	0.1253	1.1791	1.3902
	100	0	0.1180	1.1615	1.3891
Cross	5	2.9990	2.7593	2.3114	2.1717
	20	0.0290	0.2881	1.0508	1.2706
	100	0.0238	0.2743	1.0474	1.2697
Ellis	5	3.0068	3.0149	2.2115	2.0269
	20	0.0082	0.1143	1.0935	1.2923
	100	0	0.1293	1.0861	1.2800
Power-law	5	1.9235	1.7713	1.7325	1.7553
	20	1.2349	1.3856	1.4309	1.4017
	100	1.2188	1.3789	1.4164	1.3943
Newtonian	5	3.0067	3.0067	3.0067	3.0067
	20	0.0092	0.0092	0.0092	0.0092
	100	0.0033	0.0033	0.0033	0.0033

Note: The numerical integration of S_2 is conducted considering 5, 20 and 100 layers in the gapwise direction

The corresponding viscosity behavior is illustrated in Figure 8: at low shear rate the generalized viscosity models, excepting the Power-law model, exhibit a Newtonian viscosity, while at high shear rates the viscosity models are similar to Power-law behavior.

4.4 Entrance channel expansion and obstacle effects

In this test case we compare the approximation with the Newtonian fluid results in (Chang and Yang, 2001) for a rectangular channel that has a narrow entrance and a small rectangular "blockage" on the interior centerline of the mold (Figure 9). The goals

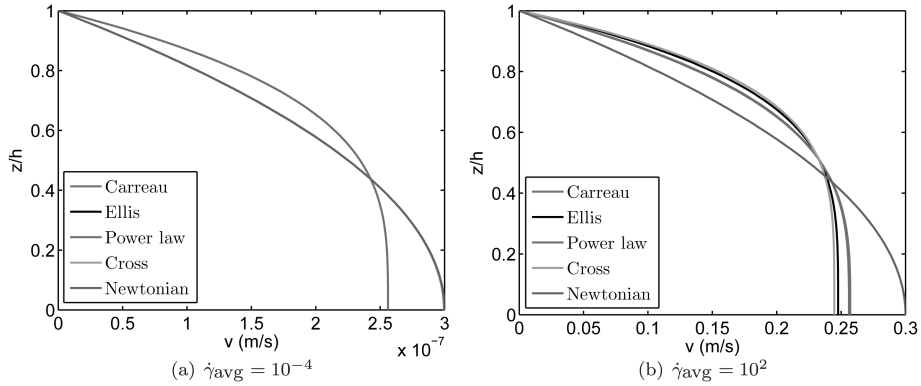

(a) $\dot{\gamma}_{\text{avg}} = 10^{-4}$ (b) $\dot{\gamma}_{\text{avg}} = 10^{2}$

Figure 7.
Velocity profiles predicted by generalized Newtonian models for polystyrene at different values of average shear rate $\dot{\gamma}_{\text{avg}}$

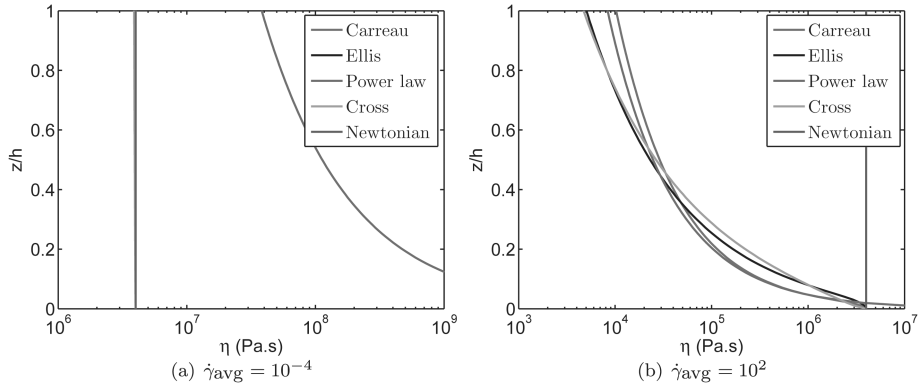

(a) $\dot{\gamma}_{\text{avg}} = 10^{-4}$ (b) $\dot{\gamma}_{\text{avg}} = 10^{2}$

Figure 8.
Viscosity profiles predicted by generalized Newtonian models for polystyrene at different values of average shear rate $\dot{\gamma}_{\text{avg}}$

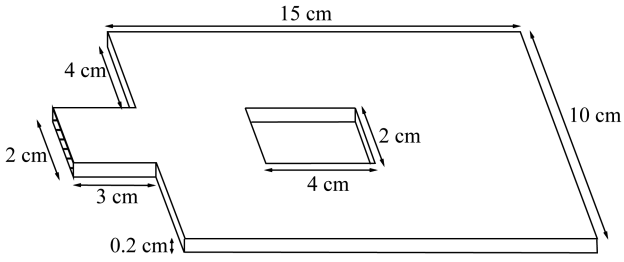

Figure 9.
Rectangular mold with an entrance channel and one insertion

are to verify the capability of the method for predicting both inlet pressure and position of the free surface for this expansion/obstacle configuration.

The pointset describing both mold boundary and interior has 608 points with interior points relatively uniformly distributed. The thickness of this mold is constant and equal to 2×10^{-3} m and the gapwise direction is divided into $N_z = 8$ layers.

Figure 10 compares the inlet pressure profile obtained for the present method with the results in (Chang and Yang, 2001) for a Newtonian fluid ($\eta_0 = 10^4$ Pa s) and inlet velocity $v_0 = 0.37$ m/s, which correspond to a filling time of 2 s, according to equation (29). The slight "bumps" in the monotone curve are due to the interaction of the front with the "obstacle".

Figure 11 depicts the position of the free surface at six different stages in mold filling: the black line represents the free surface of the fluid; the mold volume located on the left side of the black line is filled with fluid while the mold volume located on the right side of the black line is still empty. The predicted positions of the free surface agree with the results in (Chang and Yang, 2001).

The study conducted in section 4.3 compares computed inlet pressures against analytic results for a simple rectangular mold geometry with Newtonian and non-Newtonian fluids at several shear rates, while the study above compares inlet pressure profiles with computed results from the literature for a Newtonian fluid in a mold geometry with an interior boundary for which no analytic result is available.

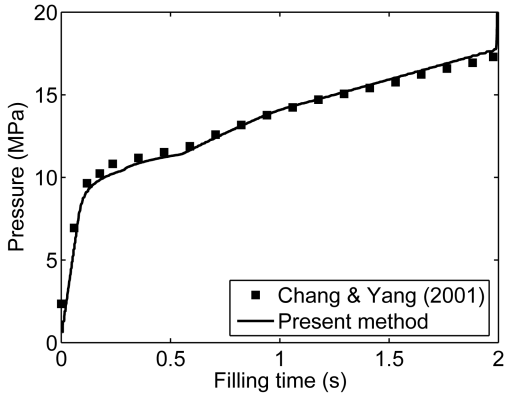

Figure 10.
Comparison of the profiles of inlet pressure for a Newtonian fluid with the 3D results of Chang and Yang (2001)

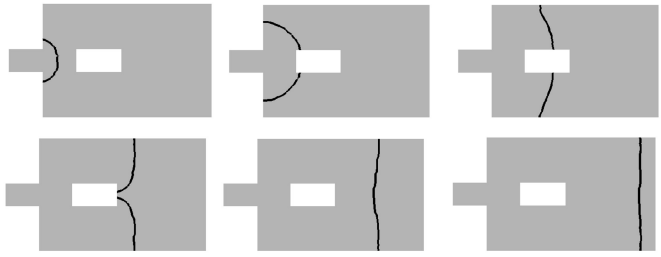

Figure 11.
Several free-surface front profiles during mold filling with a Newtonian fluid

Notes: Predicted positions are consistent with the 3D results in Chang and Yang (2001)

Now, the effect of different generalized Newtonian viscosity models on the inlet pressure results are now considered for this latter geometry under the same flow conditions for polystyrene as described in section 2.2. In this case the average value of shear rate is $\dot{\gamma}_{avg} = 1.85 \times 10^2\,s^{-1}$ and the computed inlet pressure profiles are displayed in Figure 12.

The results displayed in Figure 12 exhibit behavior that is consistent with and may be anticipated from Figure 1 and also in Table 5 for this value of shear rate. At the higher shear rate, the Cross and Ellis models behave similarly, having lower viscosity and, therefore, lower pressure than the Carreau and Power-law models, while the Carreau model has the highest values for both viscosity and pressure profiles.

Finally, the effect of the Cross, Carreau, Ellis and Power-law viscosity models on the inlet pressure is now assessed in a flow with low shear rate. A representative value of shear rate is taken as $\dot{\gamma}_{avg} = 10^{-2}\,s^{-1}$ resulting in a prescribed inlet velocity $v_0 = 2 \times 10^{-5}$ m/s. The fluid again corresponds to the previous case of polystyrene. The predicted injection time to completion of mold filling in the simulation is 36,808.61 s. Moreover, according to equation (29), the mold should be completely filled within 37,000 s, indicating a fill-time error of only 0.51 percent.

The computed inlet pressure values are again graphed against injection time for these fluids in Figure 13 as a means of displaying more clearly the effects of the distinct viscosity models at this low shear rate. Notice that Carreau and Ellis models have quite similar pressure distributions, while the pressure predicted with the Cross model is lower and the Power-law fluid exhibits larger pressure values.

According to Figure 1, at $\dot{\gamma} = 10^{-2}\,s^{-1}$, the Ellis and Carreau models exhibit similar viscosity behavior and both converge to the Newtonian plateau, while the Cross model exhibits smaller viscosity than the Newtonian value and the Power-law model exhibits a considerably larger value. This expected behavior is clearly predicted by the present method, as displayed in Figure 13. Although the use of such low prescribed inlet velocity and consequently low shear rate is not a common practice in mold-filling processes, this test case demonstrates the capability to handle simulations with these viscosity models under a range of flow conditions.

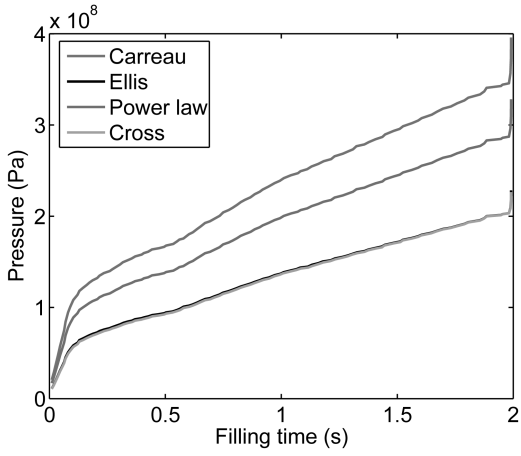

Figure 12.
Inlet pressure profiles for polystyrene during the mold filling of the rectangular mold with a narrow entrance channel using several viscosity models and prescribed inlet velocity $v_0 = 0.37$ m/s

Figure 14 shows a comparison of the velocity magnitude for the four generalized Newtonian viscosity models (white) against the Newtonian model (black) at $t = 36,808.61$ s, during the sixth stage of mold filling. Four level sets of the velocity magnitude obtained using each viscosity model are compared with the same isocontours for the Newtonian fluid. The isocontours occur when the magnitude of the velocity is equal to $1 \times 10^{-6}, 5 \times 10^{-6}, 1.5 \times 10^{-5}$ and 1×10^{-5} m/s. It can be seen that the Power-law model displays a less uniform velocity distribution than the other three models, due to the increased viscosity at low shear rate, demonstrating one of the main reasons why such a viscosity model is not appropriate in simulations with low shear rates. Carreau, Cross and Ellis present very similar curves, with smaller stagnation regions than that of the Power-law model. These results are also consistent with the data from Figure 1, for low shear rate conditions.

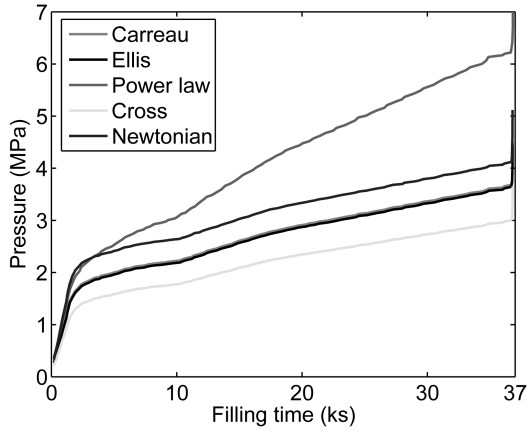

Figure 13.
Inlet pressure profiles for polystyrene during mold filling of a rectangular mold with a narrow entrance channel using several viscosity models and prescribed inlet velocity $v_0 = 2 \times 10^{-5}$ m/s

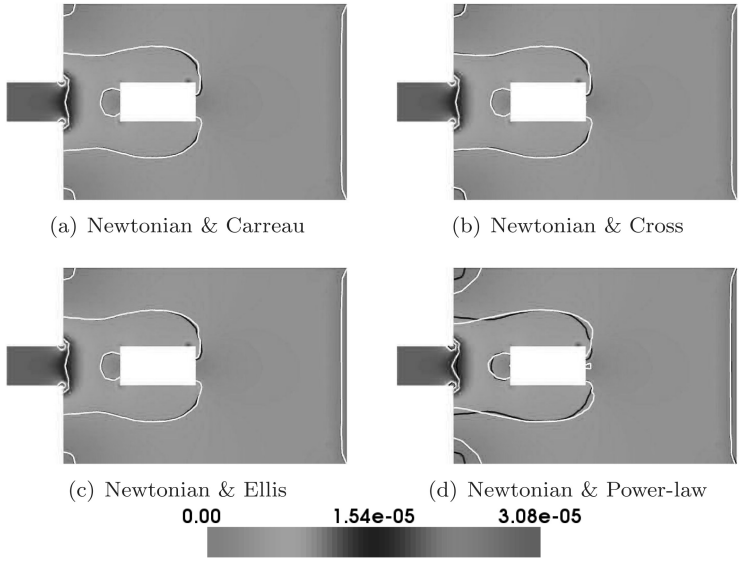

Figure 14.
Velocity magnitude and four isocontours for Newtonian (black) and generalized Newtonian (white) fluids, at $t = 35879.56\,s$

4.5 Multiply-connected geometry

In this last test case the flow domain is multiply-connected and corresponds to a rectangular mold with several geometrical interior closed boundaries similar to a mold configuration for an "electronic digital calculator." The mold thickness is constant and given by $h = 2 \times 10^{-3}$ m. A top view of the mold geometry with the inlet region represented by several arrows is shown in Figure 15. The pointset defining both mold boundary and interior has 2,063 points and the gapwise direction is divided into $N_z = 15$ layers.

The simulation study for this geometry is confined to the Cross fluid model as a representative case to illustrate the capability of the numerical scheme to deal with many splitting and merging fluid fronts in a multiply-connected domain. Also, results for inlet pressure profile and filling time estimation are compared to results provided by a different method in (Estacio and Mangiavacchi, 2007) for the same problem using a conventional discretization and data structure. The prescribed inlet velocity is $v_0 = 1.25 \times 10^{-2}$ m/s.

Figure 16 compares inlet pressure profiles for the present method and that in (Estacio and Mangiavacchi (2007), while Figure 17 depicts the free-surface position

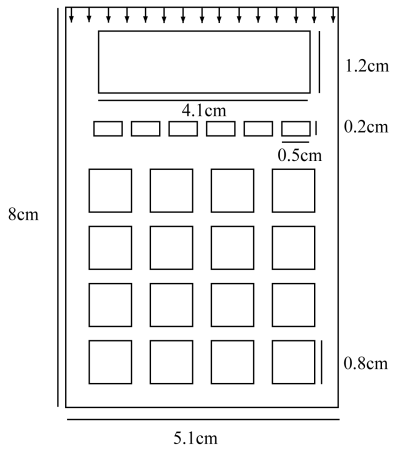

Figure 15.
Top view of mold dimensions and inlet region represented by arrows

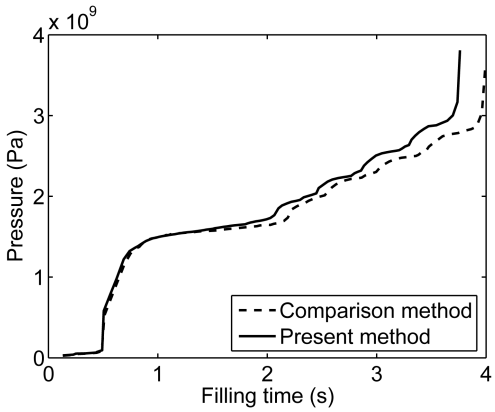

Figure 16.
Comparison of the profiles of inlet pressure through the simulation obtained by the present method with the results of Estacio and Mangiavacchi (2007)

within the mold at four times during injection, for both methods: the present method (in black) and the comparison method (in white).

There is a good agreement between the free surface position in both cases, particularly early in the simulation when the front positions are mostly indistinguishable. Figure 18 displays in detail the advance of the free surface around the "obstacles" using the present method.

A comparison of fill time is also made relative to that in (Estacio and Mangiavacchi (2007). The expected injection time is 3.9278 s, whereas the present method provides the predicted fill time of 3.8844 s for the given pointset, resulting in an error of 1.10 per cent. The previous method in Estacio and Mangiavacchi (2007) predicts 3.9919 s resulting in a comparable error in the fill time of 1.60 per cent. Errors in fill time can clearly be interpreted in terms of mass errors and the mesh refinement study presented in section 4.1 explores the rate of convergence under a relatively uniform pointset refinement in this context.

5. Concluding remarks

This work presents a novel unstructured simulation approach for injection molding processes described by the Hele-Shaw model. The discretization strategy involves dual meshes with active and inactive cells determined from an initial background pointset describing the domain and the boundary: local active dual patches are constructed "on-the-fly" for each "active point" to form a dynamic virtual mesh of active elements that

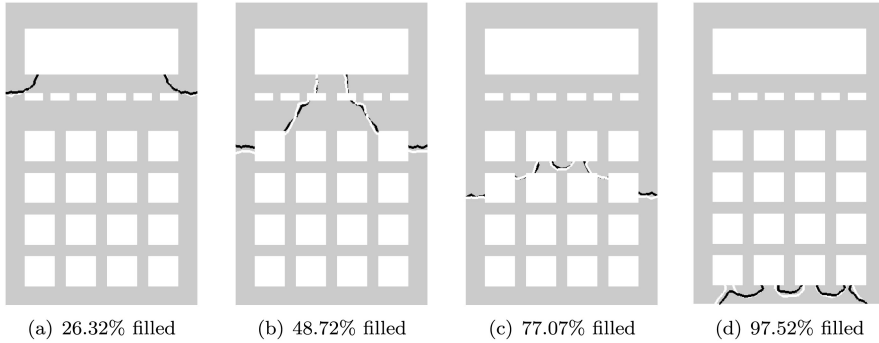

Figure 17.
Comparison between the free-surface position predicted by the present method (in black) and the method in Estacio and Mangiavacchi (2007) (in white)

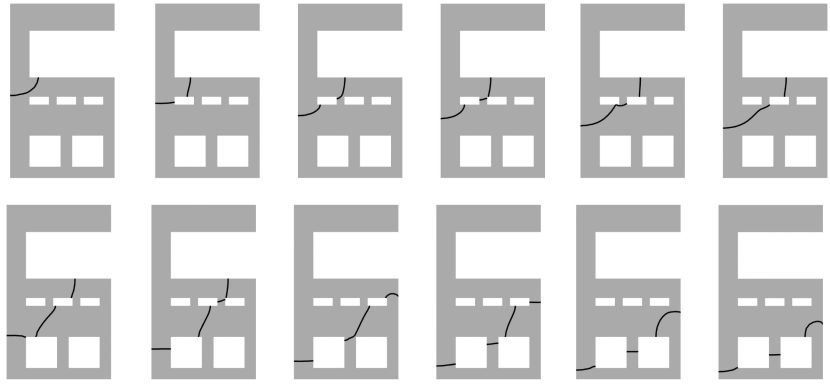

Figure 18.
Free surface advancement around the calculator insertions

evolves with the moving interface. An adaptation of the CVFEM is employed in the context of a dynamic mesh for discretizing the pressure field, while an analogous dynamic local VOF level set type of scheme is introduced in order to predict the free surface position.

Several supporting numerical tests and performance studies for isothermal flow of Newtonian and non-Newtonian fluids are conducted. First, the accuracy of the moving front algorithm and the mass-preserving accuracy indicated by "fill time" are investigated (section 4.1). Next, numerical performance results, based on operation counts, for each one of the viscosity models are compared for two pointsets (section 4.2). Further studies compare inlet pressure profiles for both simple and more complex geometry and fluids (sections 4.3 and 4.4). Finally, results for the present method are shown to be comparable to those from another method for a polystyrene fluid in a complex geometry (section 4.5).

There are still several aspects that merit further study and extension of the methodology. While in Hele-Shaw type approximations some physical effects are ignored (e.g. fountain flow (Holm and Langtangen, 1999; Kietzmann *et al.*, 1998) or cannot be predicted (recirculation zones), there are other effects that can be incorporated in our model. In particular, non-isothermal temperature effects on the fluid viscosity and subsequent cooling and solidifying phenomena are very relevant and a natural extension of the work.

Furthermore, in mold-filling simulations with strong local curvature of the front, surface tension contributions may become important, and this extension would be warranted. With respect to the methodology, the background pointset infers a mesh that is dynamically reconstructed here, and there are a number of efficiency issues and improvements that would be relevant to industrial applications. For instance, one can use the pointset to construct special bases and invoke a so-called "meshless" scheme using the basis. This would require some interesting strategies to deal with the dynamic point enrichment of the moving front that could benefit from the present front treatment strategy. There are also issues related to mass conservation and fill-time errors that might be addressed by introducing suitable projections. The general question of "rate of convergence" of these schemes requires analysis. Numerical results here suggest first-order accuracy and are consistent with the approximations made, but theoretical results are not available yet for these methods.

References

Abbassi, H., Boughamoura, A. and Nasrallah, S.B. (2003), "A comparison between linear and exponential schemes in control volume finite element method", *International Journal of Numerical Methods for Heat & Fluid Flow*, Vol. 13 No. 4, pp. 403-14.

Baliga, B.R. and Patankar, S.V. (1980), "A new finite element formulation for convection-diffusion problems", *Numerical Heat Transfer, Part A: Applications*, Vol. 3, pp. 393-409.

Baliga, B.R. and Patankar, S.V. (1983), "A control volume finite-element method for two-dimensional fluid flow and heat transfer", *Numerical Heat Transfer, Part A: Applications*, Vol. 6, pp. 245-61.

Belytschko, T., Krongauz, Y., Organ, D., Fleming, M. and Krysl, P. (1996), "Meshless methods: an overview and recent developments", *Computer Methods in Applied Mechanics Engineering*, Vol. 139, pp. 3-47.

Bernal, F. and Kindelan, M. (2007), "RBF meshless modeling of non-Newtonian Hele-Shaw flow", *Engineering Analysis with Boundary Elements*, Vol. 31, pp. 863-74.

Bridson, R. and Greif, C. (2006), "A multipreconditioned conjugate gradient algorithm", *SIAM Journal on Matrix Analysis and Applications*, Vol. 27, pp. 1056-68.

Carey, G.F. and Chow, S.S. (2003), "Numerical approximation of generalized Newtonian fluids using Powell-Sabin-Heindl elements: I. theoretical estimates", *International Journal for Numerical Methods in Fluids*, Vol. 41, pp. 1085-118.

Carey, G.F. and Jiang, B.N. (1986), "Element by element linear and nonlinear solution schemes", *Communications in Applied Numerical Methods*, Vol. 2 No. 2, pp. 145-53.

Carey, G.F. and Jiang, B.N. (1987), "Nonlinear preconditioned conjugate gradient and least squares finite elements", *Computer Methods in Applied Mechanics and Engineering*, Vol. 62, pp. 145-54.

Chang, R.-Y. and Yang, W.-H. (2001), "Numerical simulation of mold filling in injection molding using a three-dimensional finite volume approach", *International Journal for Numerical Methods in Fluids*, Vol. 37, pp. 125-48.

Chen, S.C., Chen, Y.C. and Cheng, N.T. (1998), "Simulation of injection-compression mold-filling process", *International Communications in Heat and Mass Transfer*, Vol. 25, pp. 907-17.

Codina, R. and Schãfer, U. and Oñate, E. (1994), "Mould filling simulation using finite elements", *International Journal of Numerical Methods for Heat & Fluid Flow*, Vol. 4, pp. 291-310.

Coutinho, A.L.G.A., Martins, M.A.D., Sydenstricker, R.M. and Elias, R.N. (2006), "Performance comparison of data-reordering algorithms for sparse matrix-vector multiplication in edge-based unstructured grid computations", *International Journal for Numerical Methods in Engineering*, Vol. 66, pp. 431-60.

Estacio, K.C. and Mangiavacchi, N. (2007), "Simplified model for mold filling simulations using CVFEM and unstructured meshes", *Communications in Numerical Methods in Engineering*, Vol. 23, pp. 345-61.

Estacio, K.C., Nonato, L.G., Mangiavacchi, N. and Carey, G.F. (2008), "Combining CVFEM and meshless front tracking in Hele-Shaw mold filling simulation", *International Journal for Numerical Methods in Fluids*, Vol. 56, pp. 1217-23.

Hele-Shaw, H.S. (1898), "On the motion of a viscous fluid between two parallel plates", *Transactions of the Royal Institution of Naval Architects*, Vol. 40, p. 218.

Helleloid, G.T. (2001), "On the computation of viscosity-shear rate temperature master curves for polymeric liquids", *Morehead Electronic Journal of Applicable Mathematics*, Vol. 1, pp. 1-11.

Hieber, C.A. and Shen, S.F. (1980), "A finite-element/finite-difference simulation of the injection-molding filling process", *Journal of Non-Newtonian Fluid Mechanics*, Vol. 7, pp. 1-32.

Hirt, C.W. and Nichols, B.D. (1981), "Volume of fluid (VOF) method for the dynamics of free boundaries", *Journal of Computational Physics*, Vol. 39, pp. 201-25.

Hirt, C.W., Amsden, A.A. and Cook, J.L. (1974), "An arbitrary Lagrangian-Eulerian computing method for all flow speeds", *Journal of Computational Physics*, Vol. 14, pp. 227-53.

Holm, E. and Langtangen, H. (1999), "A unified finite element model for the injection molding process", *Computer Methods in Applied Mechanics and Engineering*, Vol. 178, pp. 413-29.

Isaacson, E. and Keller, H.B. (1966), *Analysis of Numerical Methods*, Wiley, New York, NY.

Jiang, S., Wang, Z., Zhoub, G. and Yang, W. (2007), "An implicit control-volume finite element method and its time step strategies for injection molding simulation", *Computers and Chemical Engineering*, Vol. 31, pp. 1407-18.

Kennedy, P. (1995), *Flow Analysis of Injection Molds*, Hanser Publishers, New York, NY.

Kietzmann, C.v.L., Van Der Walt, J.P. and Morsi, Y.S. (1998), "A free-front tracking algorithm for a control-volume-based Hele-Shaw method", *International Journal for Numerical Methods in Engineering*, Vol. 41, pp. 253-69.

Lewis, R., Navti, S. and Taylor, C. (1997), "A mixed Lagrangian-Eulerian approach to the modelling of fluid flow during mould filling", *International Journal for Numerical Methods in Fluids*, Vol. 25, pp. 1-22.

Li, S. and Liu, W. (2002), "Meshfree and particle methods and their applications", *Applied Mechanics Reviews*, Vol. 55, pp. 1-34.

Li, X., Duan, Q., Han, X. and Sheng, D.C. (2008), "Adaptive coupled arbitrary Lagrangian-Eulerian finite element and meshfree method for injection molding process", *International Journal for Numerical Methods in Engineering*, Vol. 73 No. 8, pp. 1153-80.

Liu, G. R. (2003), *Meshfree Methods – Moving Beyond the Finite Element Method*, CRC Press, Boca Raton, FL.

Myers, T.G. (2005), "Application of non-Newtonian models to thin film flow", *Physical Review E – Statistical, Nonlinear, and Soft Matter Physics*, Vol. 72 No. 6 (Pt 2), pp. 066302–1-066302–11.

Niceno, B. (2001), "Easymesh: a free two-dimensional quality mesh generator based on Delaunay triangulation", available at: www-dinma.univ.trieste.it/nirftc/research/easymesh/ (accessed 24 November 2008).

Roy, C.J. (2005), "Review of code and solution verification procedures for computational simulation", *Journal of Computational Physics*, Vol. 205, pp. 131-56.

Shin, S. and Lee, W.I. (2000), "Finite element analysis of incompressible viscous flow with moving free surface by selective volume of fluid method", *International Journal of Heat & Fluid Flow*, Vol. 21, pp. 197-206.

Subbiah, S., Trafford, D.L. and Güçeri, S.I. (1989), "Non-isothermal flow of polymers into two-dimensional, thin cavity molds: a numerical grid generation approach", *International Journal of Heat and Mass Transfer*, Vol. 32, pp. 415-34.

Tucker III, C.L. (1989), *Computer Modeling for Polymer Processing – Fundamental. Computed Aided Engineering for Polymer Processing*, Hanser Publishers, New York, NY.

Verhoyen, O. and Dupret, F. (1998), "A simplified method for introducing the Cross viscosity law in the numerical simulation of Hele-Shaw flow", *Journal of Non-Newtonian Fluid Mechanics*, Vol. 74, pp. 25-46.

Zhou, H. and Li, D. (2001), "A numerical simulation of the filling stage in injection molding based on a surface model", *Advances in Polymer Technology*, Vol. 20, pp. 125-31.

Zhou, J. and Turing, L.-S. (2006), "Three-dimensional numerical simulation of injection molding filling with a finite-volume method and parallel computing", *Advances in Polymer Technology*, Vol. 25, pp. 247-58.

Further reading

Li, J., Hesse, M., Ziegler, J. and Woods, A.J. (2005), "An arbitrary Lagrangian-Eulerian method for moving-boundary problems and its application to jumping over water", *Journal of Computational Physics*, Vol. 208, pp. 289-314.

About the authors

Kemelli C. Estacio holds a PhD (2008) and an MSc (2004) degree in Computational Mathematics and Computer Science from the University of Sao Paulo, Brazil, and a BS (Hons.) in Mathematics (2001) from the Sao Paulo State University, Brazil. Her research focuses on numerical analysis and computational and applied mathematics, particularly in fluid flow simulations and code verification and validation. She has authored two articles in international journals and several papers in conferences. Kemelli C. Estacio is the corresponding author and can be contacted at: kemelliestacio@gmail.com

Graham F. Carey is a Member of the interdisciplinary Institute for Computational Engineering and Sciences (ICES), Professor in the Department of Aerospace Engineering and Engineering Mechanics at the University of Texas at Austin, and holder of the Richard B. Curran

Centennial Chair in Engineering. He holds PhD and MSc degrees from the University of Washington at Seattle, and a BS (Hons.) degree from University of Queensland, Australia. His research and teaching activities primarily deal with techniques in computational mechanics, particularly finite element methods and supercomputing. Graham F. Carey has authored over 200 journal articles, co-authored several books, and he is a member of the editorial boards of several journals.

Norberto Mangiavacchi is a Professor at the University of the State of Rio de Janeiro, Brazil. He holds a PhD degree in Mechanical Engineering and Scientific Computing, University of Michigan at Ann Arbor (1994), and an MSc (1988) and a BS (1983) in Mechanical Engineering from Pontifical Catholic University of Rio de Janeiro, Brazil. His research includes numerical simulation, turbulence and pseudo-spectral methods. Publications include approximately 30 papers and multiple book chapters.

To purchase reprints of this article please e-mail: **reprints@emeraldinsight.com**
Or visit our web site for further details: **www.emeraldinsight.com/reprints**